Depth-resolved wavefront aberrations using a coherence-gated Shack-Hartmann wavefront sensor

Simon Tuohy* and Adrian Gh. Podoleanu

Applied Optics Group, School of Physical Sciences, University of Kent, CT2 7NH Canterbury, UK
**simontuohy@gmail.com*

Abstract: In the present paper we investigate the possibility of narrowing the depth range of a physical Shack – Hartmann (SH) wavefront sensor (WFS) by using coherence gating. For the coherence gating, two low coherence interferometry (LCI) methods are evaluated and proof of principle configurations demonstrated: (i) a time domain LCI method based on phase shifting interferometry and (ii) a spectral domain LCI method, based on tuning a narrow band optical source. The two configurations are used to demonstrate each, the possibility of constructing a coherence gated (CG) SH/WFS. It is shown that these configurations produce spot patterns similar to those provided by a conventional SH/WFS. The two proof of principle configurations are also used to illustrate elimination of stray reflections in the interface optics which normally disturb the operation of conventional SH/WFSs. The speed and noise performance of the two CG-SH/WFS implementations are discussed.

OCIS codes: (170.4470) Ophthalmology; (170.4500) Optical coherence tomography; (170.3890) Medical optics instrumentation. (110.1080) Adaptive Optics (180.0180) Microscopy

References and links

1. D. Huang, E. A. Swanson, C. P. Lin, J. S. Schuman, W. G. Stinson, W. Chang, M. R. Hee, T. Flotte, K. Gregory, C. A. Puliafito, and J. G. Fujimoto, "Optical coherence tomography," Science **254**(5035), 1178–1181 (1991).
2. R. H. Webb, G. W. Hughes, and F. C. Delori, "Confocal scanning laser ophthalmoscope," Appl. Opt. **26**(8), 1492–1499 (1987).
3. M. Minsky, "Microscopy apparatus US patent 3013467," (Ser, 1957).
4. R. J. Zawadzki, S. M. Jones, S. S. Olivier, M. Zhao, B. A. Bower, J. A. Izatt, S. Choi, S. Laut, and J. S. Werner, "Adaptive-optics optical coherence tomography for high-resolution and high-speed 3D retinal in vivo imaging," Opt. Express **13**(21), 8532–8546 (2005).
5. A. Roorda, F. Romero-Borja, W. Donnelly Iii, H. Queener, T. Hebert, and M. Campbell, "Adaptive optics scanning laser ophthalmoscopy," Opt. Express **10**(9), 405–412 (2002).
6. M. J. Booth, M. A. A. Neil, and T. Wilson, "Aberration correction for confocal imaging in refractive-index-mismatched media," J. Microsc. **192**(2), 90–98 (1998).
7. B. Hermann, E. J. Fernández, A. Unterhuber, H. Sattmann, A. F. Fercher, W. Drexler, P. M. Prieto, and P. Artal, "Adaptive-optics ultrahigh-resolution optical coherence tomography," Opt. Lett. **29**(18), 2142–2144 (2004).
8. R. H. Webb, C. M. Penney, and K. P. Thompson, "Measurement of ocular local wavefront distortion with a spatially resolved refractometer," Appl. Opt. **31**(19), 3678–3686 (1992).
9. R. Navarro, and E. Moreno-Barriuso, "Laser ray-tracing method for optical testing," Opt. Lett. **24**(14), 951–953 (1999).
10. A. Chernyshov, U. Sterr, F. Riehle, J. Helmcke, and J. Pfund, "Calibration of a Shack-Hartmann sensor for absolute measurements of wavefronts," Appl. Opt. **44**(30), 6419–6425 (2005).
11. S. R. Chamot, C. Dainty, and S. Esposito, "Adaptive optics for ophthalmic applications using a pyramid wavefront sensor," Opt. Express **14**(2), 518–526 (2006).
12. B. C. Platt, and R. Shack, "History and principles of Shack-Hartmann wavefront sensing," J. Refract. Surg. **17**, 573–577 (2001).
13. D. U. Bartsch, M. H. El-Bradey, A. El-Musharaf, and W. R. Freeman, "Improved visualisation of choroidal neovascularisation by scanning laser ophthalmoscope using image averaging," Br. J. Ophthalmol. **89**(8), 1026–1030 (2005).

#119017 - $15.00 USD Received 29 Oct 2009; revised 11 Jan 2010; accepted 31 Jan 2010; published 3 Feb 2010

14. J. Liang, and D. R. Williams, "Aberrations and retinal image quality of the normal human eye," J. Opt. Soc. Am. A **14**(11), 2873–2883 (1997).
15. H. Hofer, P. Artal, B. Singer, J. L. Aragón, and D. R. Williams, "Dynamics of the eyes wave aberration," J. Opt. Soc. Am. A **18**(3), 497–506 (2001).
16. M. J. Booth, M. A. A. Neil, R. Juskaitis, and T. Wilson, "Adaptive aberration correction in a confocal microscope," Proceedings of the National Academy of Sciences, 82544799 (2002).
17. J. R. Fienup, and J. J. Miller, "Aberration correction by maximizing generalized sharpness metrics," J. Opt. Soc. Am. A **20**(4), 609–620 (2003).
18. P. Marsh, D. Burns, and J. Girkin, "Practical implementation of adaptive optics in multiphoton microscopy," Opt. Express **11**(10), 1123–1130 (2003).
19. D. Merino, C. Dainty, A. Bradu, and A. G. Podoleanu, "Adaptive optics enhanced simultaneous en-face optical coherence tomography and scanning laser ophthalmoscopy," Opt. Express **14**(8), 3345–3353 (2006).
20. M. Feierabend, M. Rückel, and W. Denk, "Coherence-gated wave-front sensing in strongly scattering samples," Opt. Lett. **29**(19), 2255–2257 (2004).
21. M. Rueckel, J. A. Mack-Bucher, and W. Denk, "Adaptive wavefront correction in two-photon microscopy using coherence-gated wavefront sensing," Proc. Natl. Acad. Sci. U.S.A. **103**(46), 17137–17142 (2006).
22. T. Dresel, G. Häusler, and H. Venzke, "Three-dimensional sensing of rough surfaces by coherence radar," Appl. Opt. **31**(7), 919–925 (1992).
23. A. Dubois, K. Grieve, G. Moneron, R. Lecaque, L. Vabre, and C. Boccara, "Ultrahigh-resolution full-field optical coherence tomography," Appl. Opt. **43**(14), 2874–2883 (2004).
24. S. R. Chinn, E. A. Swanson, and J. G. Fujimoto, "Optical coherence tomography using a frequency-tunable optical source," Opt. Lett. **22**(5), 340–342 (1997).
25. S. K. Dubey, T. Anna, C. Shakher, and D. S. Mehta, "Fingerprint detection using full-field swept-source optical coherence tomography," Appl. Phys. Lett. **91**(18), 181106 (2007).
26. J. E. Greivenkamp, and J. H. Bruning, "Phase shifting interferometry," Optical Shop Testing, 501–599 (1992).
27. M. Choma, M. Sarunic, C. Yang, and J. Izatt, "Sensitivity advantage of swept source and Fourier domain optical coherence tomography," Opt. Express **11**(18), 2183–2189 (2003).
28. M. V. Sarunic, S. Weinberg, and J. A. Izatt, "Full-field swept-source phase microscopy," Opt. Lett. **31**(10), 1462–1464 (2006).
29. G. Häusler, and M. W. Lindner, """"Coherence Radar" and "Spectral Radar"—New Tools for Dermatological Diagnosis," J. Biomed. Opt. **3**(1), 21 (1998).
30. K. Grieve, A. Dubois, M. Simonutti, M. Paques, J. Sahel, J. F. Le Gargasson, and C. Boccara, "In vivo anterior segment imaging in the rat eye with high speed white light full-field optical coherence tomography," Opt. Express **13**(16), 6286–6295 (2005).
31. D. R. Neal, J. Copland, and D. A. Neal, "Shack-Hartmann wavefront sensor precision and accuracy," in *Proc. of SPIE, ser. Advanced Characterization Techniques for Optical, Semiconductor, and Data Storage Components* (2002), pp. 148–160.
32. D. Hammer, R. D. Ferguson, N. Iftimia, T. Ustun, G. Wollstein, H. Ishikawa, M. Gabriele, W. Dilworth, L. Kagemann, and J. Schuman, "Advanced scanning methods with tracking optical coherence tomography," Opt. Express **13**(20), 7937–7947 (2005).
33. M. Pircher, B. Baumann, E. Götzinger, H. Sattmann, and C. K. Hitzenberger, "Simultaneous SLO/OCT imaging of the human retina with axial eye motion correction," Opt. Express **15**(25), 16922–16932 (2007).
34. R. G. Cucu, M. W. Hathaway, A. G. Podoleanu, and R. B. Rosen, "Active axial eye motion tracking by extended range closed loop OPD-locked white light interferometer for combined confocal/en face optical coherence tomography imaging of the human eye fundus in vivo," (2009), p. 73721R.
35. J. Batlle, J. Mart, P. Ridao, and J. Amat, "A new FPGA/DSP-based parallel architecture for real-time image processing," Real-Time Imaging **8**(5), 345–356 (2002).
36. R. Huber, D. C. Adler, V. J. Srinivasan, and J. G. Fujimoto, "Fourier domain mode locking at 1050 nm for ultra-high-speed optical coherence tomography of the human retina at 236,000 axial scans per second," Opt. Lett. **32**(14), 2049–2051 (2007).
37. Y. Watanabe, and T. Itagaki, "Real-time display on Fourier domain optical coherence tomography system using a graphics processing unit," J. Biomed. Opt. **14**(6), 060506 (2009).
38. S. Makita, T. Fabritius, and Y. Yasuno, "Full-range, high-speed, high-resolution 1-μm spectral-domain optical coherence tomography using BM-scan for volumetric imaging of the human posterior eye," Opt. Express **16**(12), 8406–8420 (2008).
39. A. Gh, Podoleanu, R. G. Cucu, R. B. Rosen, G. M. Dobre, J. A. Rogers, D. A. Jackson, and V. R. Shidlovski, "Adjustable coherence length sources for low-coherence interferometry," (Proc of SPIE; 2002), pp. 116–124.
40. E. J. Fernández, B. Hermann, B. Považay, A. Unterhuber, H. Sattmann, B. Hofer, P. K. Ahnelt, and W. Drexler, "Ultrahigh resolution optical coherence tomography and pancorrection for cellular imaging of the living human retina," Opt. Express **16**(15), 11083–11094 (2008).
41. R. E. Bedford, and G. Wyszecki, "Axial chromatic aberration of the human eye," J. Opt. Soc. Am. **47**(6), 564–565 (1957).
42. E. Fernández, A. Unterhuber, P. Prieto, B. Hermann, W. Drexler, and P. Artal, "Ocular aberrations as a function of wavelength in the near infrared measured with a femtosecond laser," Opt. Express **13**(2), 400–409 (2005).

#119017 - $15.00 USD Received 29 Oct 2009; revised 11 Jan 2010; accepted 31 Jan 2010; published 3 Feb 2010

43. M. A. Vorontsov, G. W. Carhart, M. Cohen, and G. Cauwenberghs, "Adaptive optics based on analog parallel stochastic optimization: analysis and experimental demonstration," J. Opt. Soc. Am. A **17**(8), 1440–1453 (2000).

1. Introduction

The quality of images collected by established imaging techniques such as Optical Coherence Tomography (OCT) [1], Scanning Laser Ophthalmoscopy (SLO) [2] and confocal microscopy [3] have been improved in recent years by the introduction of adaptive optics (AO) [4–7]. Generally these systems have three components, a wavefront sensor (WFS), a corrector and a control system. Different types of WFSs are known, subjective, such as using a refractometer [8] and objective, such as laser ray tracing [9], Shack – Hartmann (SH) [10] and pyramid wavefront sensors [11]. Such WFSs, sample the transversal distribution of aberrations. None of the WFSs mentioned above can provide depth resolved wavefront information.

The most widely used wavefront sensing device is a Shack-Hartmann wavefront sensor (SH/WFS). Incoming light is split into separate spatial windows by each lenslet in a lenslet array and focused onto a CCD array. Each lenslet intercepts a small portion of the incoming wavefront, whose tilt from a planar wavefront leads to deviation of the focused beam behind each lenslet [12]. Some limitations of the conventional SH/WFS are discussed below, as a motivation for the development of improved such sensors, incorporating the principle of coherence gating.

2. Limitations of conventional Shack-Hartmann wavefront sensing

2.1. Insensitivity to depth variations of aberrations

Due to the limited numerical aperture (NA) in the beams associated with each microlens in the lenslet array, a SH/WFS has little sensitivity to the position in depth in the object where the signal comes from. This makes the SH/WFS insensitive to depth variations of aberrations, or more precisely, the spots are deviated from the ideal wavefront grid by quantities which represent averages of aberrations over the depth of focus of the equivalent confocal microscopy channel associated to each microlens in the lenslet array. Acquisition of depth resolved aberration would be especially important in microscopy, where shallow layers deteriorate the wavefront for successive deeper layers.

2.2. Sensitivity to stray reflections

Due to the low NA of each channel in the SH/WFS, stray reflections from the interface optics cannot be rejected and therefore supplementary spatial filters need to be employed in the interface optics. However, when imaging the eye, reflections from the cornea and eye lens cannot be entirely attenuated using spatial filters.

In order to reduce the effect of the cornea reflections, different methods have been suggested, such as: (i) moving the lenses and mirrors in the interface optics off axis [13]; (ii) using a polarization beam splitter to eliminate specular reflections [14] and (iii) off-axis illumination of the retina so that the light coming back from the retina is along a different path than that followed by the back reflections [15]. However, all these methods present disadvantages, (i) leads to further aberrations, (ii) produces signal loss and dependence on the polarization of the sample whereas (iii) requires separation of imaging and WFS paths and two optical sources.

In microscopy, multiple facets of multielements in the microscope objective and multiple reflections in the microscope slide produce strong stray light onto the CCD [16] of the SH/WFS. Even if such stray reflections do not saturate the camera in the WFS, they create additional spots to the useful spot pattern which confuse the WFS software. There is no way to distinguish the spots from the sample from those due to the interface optics, such as reflections from the microscope objective, microscope slide in microscopy or from the cornea in an SLO.

#119017 - $15.00 USD Received 29 Oct 2009; revised 11 Jan 2010; accepted 31 Jan 2010; published 3 Feb 2010

For microscopy, direct wavefront sensing was deemed unsuitable [16] and algorithms to maximize sharpness metrics have been devised to infer the correction required, such as simulated annealing or genetic algorithms. However these algorithms can take several minutes for each point on the scanning beam [17,18] to find the optimum set of voltages to be applied to the corrector. The coherence gating method proposed here allows incorporation of WFS principles with microscopy, with the advantage of quicker correction which could make microscopy of faster events possible. The problem of stray reflections in AO based imaging systems of the retina favors single path correction configurations where a thin beam is sent to the eye and aberrations are picked up by the emerging beam coming out of the eye. In this case, if only one source is to be used for both imaging and WFS measurement, then the imaging operation and the collection of aberrations are sequential. Therefore, the correction cannot be applied dynamically, as described in [7] where a flying spot system was used, and the two channels, OCT and AO worked sequentially. To perform dynamically, further complication of the system was required in working at different wavelengths via dichroic filters. It would be desirable to operate in a double path correction [4,19], where aberrations in the path going, as well as in the path coming from the object are acquired and corrected as the same beam is shared by both the SH/WFS and the imaging system. In addition, the process of acquisition of aberration information could be performed simultaneously with the imaging process. Therefore, if double path correction is targeted, then in order to avoid stray reflections in the interface optics of fundus cameras, SLOs or OCTs, curved mirrors must be used between the transversal scanner and the object, which leads to a large layout [5] and increased cost. In this case, on-axis corneal reflection is still a problem, addressed again by off-axis illumination.

Therefore, a solution for eliminating or at least reducing the intensity of stray reflections would be to improve the depth selection of the WFS.

3. Methods

Elimination of stray reflections and operation as a depth resolved WFS can be achieved by incorporating principles of coherence gating.

3.1. Using a virtual lenslet array

The first combination of low coherence interferometry and wavefront sensing principles was presented in [20] where the phase of the 3D distribution of the scattered wave was analyzed interferometrically. Further, the 3D data was virtually separated into spatial arrays corresponding to virtual SH apertures. Based on the same principle, a depth resolved WFS has been implemented for Multi-Photon Microscopy [21]. A low coherence interferometer was used and the interference pattern acquired using a CCD camera. This pattern was subsequently numerically propagated through a virtual lenslet array to create a pseudo spot diagram.

This method requires several processing steps: (i) provision of a complex amplitude image by processing interference images acquired at several phase shifts, (ii) splitting the CCD area into 441 sub-areas corresponding to virtual microlenses of 15x15 pixels and calculating the Fourier transformation over each such microlens area, which also requires a process of zero-padding and (iii) centroiding and wavefront reconstruction [21], which makes the method computationally intensive. A normal SH/WFS would only perform the latest step. The methods has 2π ambiguity and therefore requires phase unwrapping which adds to the processing time. The procedure was subject to cross talk between pixels, which alters the phase information. These deficiencies restricted the development of the method. The move from interferometric to Shack-Hartmann sensing was motivated by the need to avoid phase unwrapping and the phase instability problem of interfering sensors.

#119017 - $15.00 USD Received 29 Oct 2009; revised 11 Jan 2010; accepted 31 Jan 2010; published 3 Feb 2010

3.2. Using a physical lenslet array

In the present paper we propose and demonstrate a different solution. We investigate the utilization of a physical lenslet array as in any SH/WFS and where interference was produced after the object beam was passed through the lenslet array and thus eliminating the second step used in the virtual lenslet array method, which reduces the computational demand. The multiple beamlets output by the lenslet array are superposed on a reference beam provided by the same optical source. Due to the aberrations encountered, the beamlets suffer various deflections and the system needs to ensure that irrespective of such deviations, interference with the reference beam still takes place. In this respect, two versions of coherence gated (CG) wavefront sensors are evaluated: (i) a time domain (TD) version, driven by a source with large bandwidth and using principles of phase shifting interferometry [22,23] and (ii) a spectral domain version using a swept narrow band source (SS) [24]. The second possibility takes advantage of the recent advance in SS-OCT using a 2D camera [25] and provides supplementary advantages such as dynamic spectral compensation of focus change. The two approaches are different in their outcome and utilization:

(i) Using a broadband source, phase shifting interferometry is used to recover an *en-face* image of the spot pattern;

(ii) Under swept source illumination, A-scans are produced and therefore to generate an *en-face* image for the spot pattern, multiple A-scans are collected to sample a whole volume of the tissue which is then subsequently software cut perpendicularly to the direction of the A-scans.

The differences between the two coherence gated Shack-Hartmann Wavefront Sensors (CG-SH/WFS) versions will be discussed further below. In the following we present experiments on these two possible implementations of a CG-SH/WFS and discuss their possible applications. These can vary from (i) providing depth resolved aberrations in the sample to (ii) elimination of stray reflections in the system. In the later case, the depth variation of aberrations in the sample is ignored and aberrations introduced by the imaging system are eliminated only. We will discuss these aspects with reference to two objects, the retina and microscopy samples. We will prove the capability of the two versions of CG-SH/WFSs to eliminate stray reflections. We will also evaluate the centroiding accuracy and discuss the S/N ratio of the two methods proposed. By the end we will discuss various avenues to improve the acquisition speed and design criteria depending on the application and on the level of depth resolution required.

4. Experimental set-ups to investigate coherence gating applied to a SH/WFS using a physical lenslet array

Experiments are described below to investigate the interference conditions of an object beam output from a lenslet array with a reference beam, where the two beams are superposed via a beamsplitter. The schematic diagram to perform such a study is shown in Fig. 1. A Michelson interferometer set-up is illuminated using an optical source, OS. Light from the OS is sent via a focus element, an achromatic lens, L1, towards a beamsplitter, BS1. This splits the incoming beam into an object arm, towards a beamsplitter BS2 and into a reference arm, towards a reference mirror RM via a neutral density filter RND. In the object arm, the light passes through lenses L2, L3. These are used to increase the size of the beam diameter from 3 mm to 15 mm in order to match the aperture of a deformable mirror, DM. The DM was used here as an object, to simulate real situations of different wavefront distortions, in order to test the CG-SH/WFS. An Imagine Eyes Mirao 52d, with 52 pistons was used as DM, with a maximum stroke of ± 50 μm of tip/tilt. The light reflected off the DM was deflected by beamsplitter BS2 to a lenslet array LA, where the light was spatially divided. The LA was from Welch Allyn, with 7.5 mm focal length lenslets placed in a square with a 200 μm pitch.

#119017 - $15.00 USD Received 29 Oct 2009; revised 11 Jan 2010; accepted 31 Jan 2010; published 3 Feb 2010

The object beam output from the lenslet array, LA was superposed on the reference beam via a beamsplitter BS3. The reference beam was brought towards BS3 via a mirror M1. The SH spots suffer lateral deviations depending on the aberrations in the object beam, as with any conventional SH/WFS. These multiple beams were focused on a CCD array. The diameter of the object and the reference beams were such to illuminate more then 15 x 15 lenslets. In order to ensure that interference can take place on any pixel in the photodetector array of the CCD, all pixels need to be illuminated uniformly by the reference beam, therefore this beam was collimated. In this simplified set-up, collimation of the reference beam was determined by the lens L1. The focal length of the lenses in the LA are too small to allow for the size of the beamsplitter BS3, therefore the multiple beams created by the LA and the reference beam are projected on the CCD via a telescope formed by lenses L4 and L5. The CCD was a Retiga-Exi CCD camera from Qimaging, of 12-Bits and 6.45 µm x 6.45 µm pixel size.

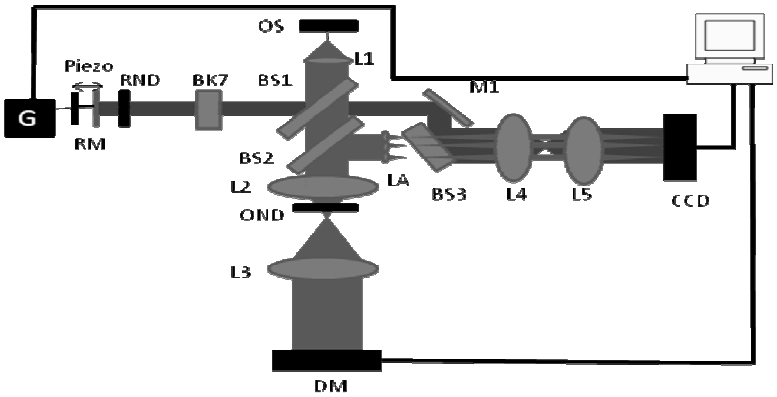

Fig. 1. Schematic diagram for the evaluation of interference between multiple beams produced by a lenslet array and a collimated reference beam. OS: optical source; OND: neutral density filter in the object path; RND: neutral density filter in the reference path; RM: reference mirror; BS1 and BS2: 50/50 beam splitters; BS3: 55/45 Beam splitter; LA: Lenslet Array; BK7: dispersion compensating glass; DM: Deformable Mirror; L1: 10x microscope objective; L2: 3 cm focal length lens; L3: 15 cm focal length lens; L4 and L5: 7.5 cm focal length lenses.

A strong reflection due to the lens L2 was present and this was used to investigate the capability of the CG-SH/WFS to provide SH spots undisturbed by the reflection in two different implementations: (i) time domain- (TD-) low coherence tomography (LCI) and (ii) spectral domain, swept source (SS-) LCI. A neutral density filter, OND, was inserted into the object arm to replicate real conditions of weakly reflecting objects and adjusted to make the intensity of the light back reflected from DM, comparable to the intensity of the stray reflection from lens L2.

4. 1. TD-LCI configuration

In the TD-LCI configuration, the source OS was a Super Luminescent Diode (SLD) from Superlum, with a central wavelength of 831 nm and FWHM bandwidth of 17 nm, possessing a coherence length of ~13 microns in the low coherent interferometer. In the reference arm, the reference mirror RM was mounted on a piezo actuator, driven by a ramp generator, G. This was used to translate RM a distance equal to the central wavelength, λ and sent a trigger signal to the computer controlling the CCD to synchronize the image acquisition. The Piezo was moved to create phase differences equal to $2\pi/m$, where m was the number of images collected during a 2π cycle at even intervals. In the work presented here m = 4 was used and the interference pattern discerned from the following equation:

$$I_D = \sqrt{(I_1(x,y) - I_3(x,y))^2 + (I_4(x,y) - I_2(x,y))^2} \quad (1)$$

#119017 - $15.00 USD Received 29 Oct 2009; revised 11 Jan 2010; accepted 31 Jan 2010; published 3 Feb 2010

where I_m was the intensity distribution in the mth image taken. Based on principles of phase shifting interferometry [26], light originating from outside the coherence gate was eliminated and the amplitude of interference from points within the coherence length is recovered [22]. Images of 400x400 pixels^2 size were produced.

4.2. SS-LCI configuration

In this case, OS was a swept source. A Superlum broad sweeper was used, with a variable sweeping rate of up to 10,000 nm/s, a tuning bandwidth of $\Delta\lambda$ = 50 nm from 820 nm to 870 nm and a linewidth of 0.05 nm. In comparison with the TD-LCI concept presented above, the SS-LCI method provides more signal to noise ratio and allows increased speed [27]. However, this method has the drawback that requires a supplementary step in comparison to the TD method, that of organizing the data in the form of an *en-face* image.

The acquisition was carried out by treating every CCD pixel as a separate photo detector [28]. As the source swept through its tuning range, a number of images were taken. To create the volume, a frame was collected for every frequency step of the SS. The limiting factor of the acquisition is the frame rate of the camera, the desired depth range and the processing speed of the computer. The fewer and smaller the frames used, the faster the measurement process, hence, for this configuration a smaller image size of 200 x 200 pixels^2 was used. The axial range of the SS-LCI is determined by the maximum of the following two quantities: (i) the source linewidth and the (ii) step in optical frequency resulting from division of the tuning bandwidth by the number of frames. In our case the frequency step from frame to frame was much larger than the linewidth, therefore the number of frames was the parameter which determined the depth range. The camera collected frames at a rate of 40 Hz.

After Fourier transformation, the DC signal resulted in a peak at the origin of the spectrum coordinate. Its width dictates the distance away from optical path difference (OPD) = 0 where other peaks can still be resolved. The larger the number of frames, the narrower the DC peak. After all M frames (X,Y) were acquired, they were stored in a 3D array. The data in this 3D array was inverse FFT transformed along the M^{th} dimension for all values of (X,Y) pixels and the results were placed into another 3D array with the same (X,Y) dimensions, whereas the M coordinate is now replaced by the axial distance, Z. From this volume of data, it is possible to retrieve an *en-face* image by computationally slicing the 3D volume at a selected axial depth δZ. Let us say that the CCD array uses PxP pixels. The 3D wavefront information can be obtained by proceeding along the following steps:

1. According to principles of SS-LCI, for each pixel (X,Y) where X = 1 to P and Y = 1 to P, an A-scan was inferred by tuning the OS within the bandwidth $\Delta\lambda$ and Fourier transforming the signal generated during such tuning. If the source was tuned within an interval $\Delta\lambda$ and M frames (for M different optical frequencies) are acquired, then Fourier transformation (FFT) of the M samples of the photodetected signal delivered an A-scan from an axial range of approx.: $\Delta Z = 0.25M\lambda^2/(\Delta\lambda)$ [29] with an axial resolution of approx.: $\lambda^2/\Delta\lambda$. If the samples collected within each scan are not for equidistant values of optical frequency, then a linearization and interpolation procedure was required before the FFT, with the possibility mentioned in paragraph 6.1. of skipping this procedure if the axial depth δZ chosen is shallow. The selection of the operating depth is further discussed in paragraph 5.4.

2. Using the PxP = 200x200 A-scans such collected in 1 second, a 3D volume, V_a was generated, consisting of PxPxM = 200x200x40 pixels^3;

3. From the volume V_a, a number of *en-face* frames were inferred, each containing corresponding deviated spots, which determine the aberration information for a given depth value within the volume V_a of the object;

#119017 - $15.00 USD Received 29 Oct 2009; revised 11 Jan 2010; accepted 31 Jan 2010; published 3 Feb 2010

4. In each such frame, deviations of the SH spots from the reference grid can be evaluated to provide the slopes as in any conventional SH/WFS.

5. Results

5.1. Rejection of stray light

In this paragraph, the efficiency of the two CG-SH/WFS methods in attenuating the stray light was evaluated comparatively with the standard method. In an initial measurement step, SH spots were obtained with the reference beam blocked, these correspond to the standard method. Then, with the reference beam on, the two interference methods mentioned above were used to obtain SH spots.

5.1.1. TD-LCI configuration

The optical source was the SLD and four steps of phase shifts were used as described above. Figure 2 shows the SH spots on the CCD camera. The images in the top raw were obtained with the DM flat, while the images on the bottom raw were obtained with the DM deformed by applying - 0.18 V to its electrode number 30. Images in the left column were obtained with the reference arm blocked and therefore the SH spots correspond to a conventional SH/WFS. These images contain SH spots due to the stray reflections from lens L2 (seen as thick diagonal small traces), superposed on the SH spots created by the object, DM.

The images in the right column were obtained with the reference beam on and after using the phase shifting method according to Eq. (1). These images represent spatial cropping of spots as determined by the coherence gate. The SH spots due to reflections from lens L2 were totally eliminated and the only SH spots in the image are due to the object. If the reference arm is blocked and the same phase shifting algorithm was applied, most of the SH spots disappeared, apart from small remnants due to random shot noise. All images had 400 by 400 pixels, the camera was run at 10 Hz and the system provided an *en-face* image of SH spots (after phase shifting) at 2.5 Hz. Furthermore, when working with 200 by 200 pixels^2, the camera operated at 40 Hz and an *en-face* image of SH spots could be delivered at 10 Hz. Using a camera with a higher frame rate could increase the acquisition speed even further [30].

5.1.2. SS-LCI configuration

In this case, the optical source used was the Superlum sweeper and the procedure of operation is that described in paragraph 4.2 above. The tuning was performed at 1 Hz with the 40 frames taken at evenly spaced intervals, for simplicity. This introduced some loss of sensitivity due to the frequency intervals not being equal, however tolerated here when working at small values of OPD (as commented in paragraphs 5.4 and 6.1 below).

Images obtained are shown in Fig. 3. The distribution of the back reflections differ from Fig. 2 to Fig. 3 due to the two set-ups, TD-LCI and SS-LCI, having been implemented at different times.

#119017 - $15.00 USD Received 29 Oct 2009; revised 11 Jan 2010; accepted 31 Jan 2010; published 3 Feb 2010

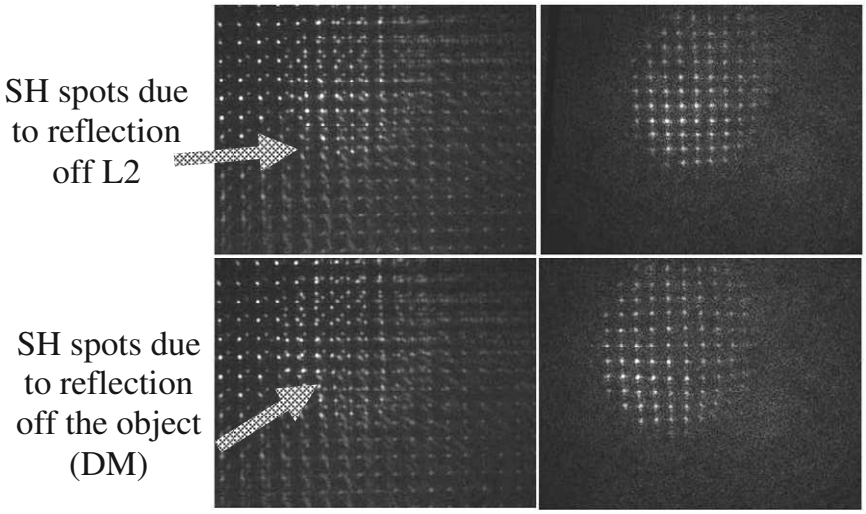

Fig. 2. Images in the top row were of the SH spots with no deformation of the mirror. Images in the bottom row were obtained with further aberrations introduced by deforming the DM, obtained by applying –0.18 V on electrode 30 of the DM. Images in the left column were obtained with the reference arm blocked and according to the conventional procedure in a SH/WFS while in the right column, images were obtained based on the principle of the TD CG-SH/WFS explained in paragraph 4.1.

As it can be seen in Fig. 3, the stray reflections from L2 are visible in the left image from middle to its top as thick diagonal small traces. The bright round points are due to reflections off the object (DM). Both patterns represent SH spots due to reflections off a wide depth interval determined by the confocal channel at the core of each lenslet, which is over several mm. On the right, an *en-face* image is shown, inferred from a stack of 40 frames obtained while tuning the wavelength of the SS, each frame acquired at a different wavelength within the tuning range of the SS. Its thickness is only 20 microns, corresponding to the inverse of the tuning bandwidth of the SS. The stray reflections are totally eliminated and SH spots due to the object only are left in the image. Slopes to infer the wavefront can be evaluated undisturbed by stray reflections from the clean SH spots.

The SH spot patterns generated by the CG-SH/WFS for different deformations of the DM looked qualitatively similar to those obtained by the SH/WFS alone, as illustrated above for the TD case, therefore they are not shown in Fig. 3.

Using a Pentium 4, 2.25 GHz, 2.25 GB RAM, an *en-face* slice of 200 x 200 pixel^2 was produced from the data cube of 40 images in 2.1 s.

#119017 - $15.00 USD Received 29 Oct 2009; revised 11 Jan 2010; accepted 31 Jan 2010; published 3 Feb 2010

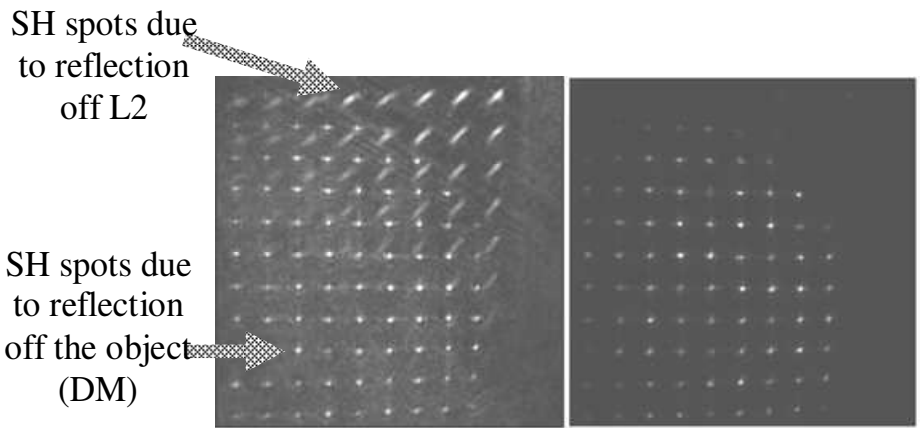

Fig. 3. Left: CCD images collected for a fixed wavelength λ = 834 nm and with the reference arm blocked. This shows the stray reflections from the lens L2 as thick diagonal small traces superposed on the reflection due to the object. Right: reference beam on, *en-face* image inferred from a stack of 40 frames, each obtained at a different wavelength within the tuning range of the SS and according to the procedure described in 4.2. The stray reflections are totally eliminated.

5.2. Enhanced signal

Another advantage of the CG-SH/WFS is that of stronger signal than that delivered by the standard SH/WFS due to the heterodyne principle implemented in the two configurations, where the weak signal from the object is multiplied by the strong signal from the reference arm. The purpose of this section is to illustrate the difference in signal strength from the different configurations investigated, TD-LCI and SS-LCI. Signals collected along a line in the middle of the CCD were compared, without the reference beam and again with the reference power on and using specific signal processing, characteristic for the two CG methods studied.

5.2.1. TD-LCI configuration

The signal sensitivity enhancement of a CG-SH/WFS using TD-LCI relative to a conventional SH/WFS is depicted in Fig. 4. The signals were collected along a line in the middle of the CCD, without the reference beam (gray line) and again with the reference power on and employing 4-step phase shifting (dashed dark line). Peaks due to back-reflections (arrow) were eliminated.

Considering the attenuation of the object and reference neutral density filters as OND and RND, respectively, the reflectivity of the object as O, the signal in the conventional SH/WFS is:

$$S_{Conv} = OND^2 \cdot O \tag{2}$$

Considering the reflectivity of the reference mirror, RM, as R, the amplitude of the interference signal is:

$$S_{CG} = \sqrt{OND^2 \cdot O \cdot RND^2 \cdot R} \approx OND \cdot RND \tag{3}$$

where the approximation in the 2nd form was allowed by considering the reflectivities O and R as 1. Evaluating the ratio of Eq. (3) to Eq. (2) leads to:

$$\frac{S_{CG}}{S_{conv}} = \frac{RND}{OND} \tag{4}$$

#119017 - $15.00 USD Received 29 Oct 2009; revised 11 Jan 2010; accepted 31 Jan 2010; published 3 Feb 2010

The images in Fig. 2 and 4 were obtained with an OND transmitting 1% round trip and a RNDF transmitting 3% roundtrip. This leads to:

$$(\frac{RND}{OND})^2 = \frac{3}{1} \approx 3 \text{ and } \frac{S_{CG}}{S_{conv}} = \sqrt{3} \approx 1.73 \quad (5)$$

Experimentally, a value of 2 of the improvement in the signal strength was obtained in several places, as shown in Fig. 4, close to the approximation above.

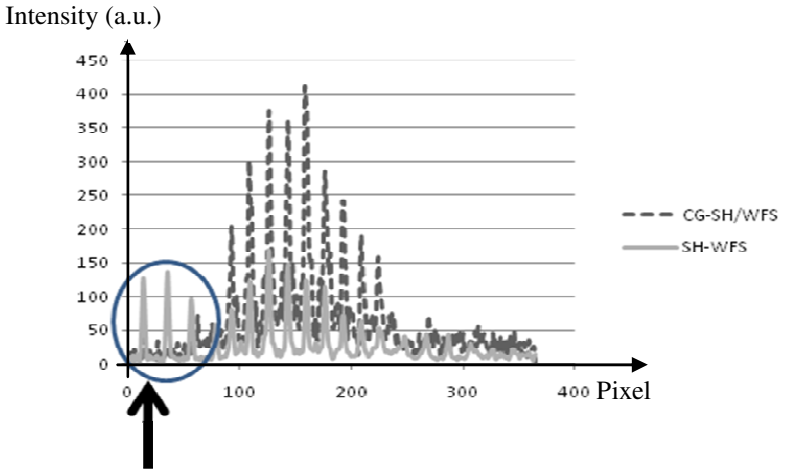

Fig. 4. Comparison of signal sensitivity of conventional SH/WFS versus CG-SH/WFS using TD/LCI. The peaks in the left bottom corner represent stray reflections totally eliminated when performing coherence gating.

5.2.2. SS-LCI configuration

The strength enhancement has been quantified in Fig. 5. The signal amplitude was collected along a line in the middle of the CCD, without the reference beam (gray line) and again in the final *en-face* image, obtained with the reference power on, tuning the SS, collecting the data for all pixels, performing FFT to produce A-scans followed by sectioning at the selected δz to infer the *en-face* (dashed dark line). The amplitude of the signal is greater than that of the standard SH/WFS in several places by a factor of 2 to 10. It can also be noticed that peaks due to back-reflections (arrow) are eliminated. According to [27], the interference signal strength in SS-LCI should increase by a factor of M/4, where M is the number of spectral windows, while the noise is the same as in TD-LCI. Here the number of frames, 40, would give an improvement factor of 10 in comparison with the signal in TD-LCI (and hence the same improvement for the S/N ratio). Considering as reference value the strength of the conventional SH/WFS signal, the improvement can be estimated as the ratio of the signal strength enhancements in Figs. 5 and 4, i.e. 10/2 = 5. The improvement is less than that estimated theoretically for some of the peaks and this may have different explanations, as commented later. The speckle however is ruled out, as similar results were obtained by repeating the procedure.

#119017 - $15.00 USD Received 29 Oct 2009; revised 11 Jan 2010; accepted 31 Jan 2010; published 3 Feb 2010

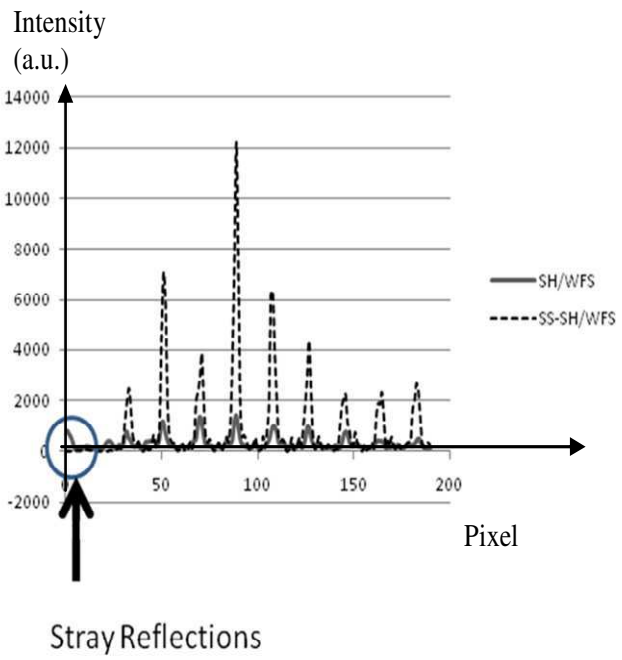

Fig. 5. SS-LCI. (**C**)omparison of signal sensitivity of conventional SH/WFS versus CG-SH/WFS using SS/LCI. The peaks in the left bottom corner represent stray reflections totally eliminated when performing coherence gating.

In conclusion, an enhancement of the signal was obtained using both coherence gated methods. However, a better characterization of sensitivity should be performed in terms of S/N. Noise levels are higher in the interference images than in the single shot images without a reference beam. However, the noise could be reduced by increasing the number of steps used in the TD phase shifting interferometry method and the number of frames in the SS method, with the disadvantage that the acquisition speed may suffer. Relevant for the comparison of S/N of the two configurations are prior studies on comparing the SS-OCT with TD-OCT [26].

A S/N ratio comparison was also performed. The noise was evaluated as the ac fluctuation on pixels well outside the spots. The maximum signal was evaluated as an average over peaks in the line acquired in Fig. 4 and 5. For the particular cases exemplified here, the S/N in the TD case was 2 dB higher than the standard SH/WFS and 9 dB higher in the SS case than in the standard SH/WFS.

5.3. Centroiding accuracy

5.3.1. Comparison between SH spots in the conventional SH/WFS and in the two versions of CG-SH/WFSs

Functionality of the CG/WFS can only be proven by demonstrating that the CG principle does not affect the wavefront measurements. To this goal, the SH spots obtained by using the conventional SH/WFS and the two versions of CG-SH/WFS should be compared. Unfortunately, we deliberately exacerbated the stray reflections to test the capability of the CG/WFS in removing them. They are so strong, that the wavefront cannot be measured using the images obtained using the conventional SH/WFS. As seen in Fig. 2 left and Fig. 3 left, it is difficult to say which are the SH spots due to the object and which are the SH spots due to the stray reflections. Therefore, we first separated the SH spots using two or more frames

#119017 - $15.00 USD Received 29 Oct 2009; revised 11 Jan 2010; accepted 31 Jan 2010; published 3 Feb 2010

obtained for different deformations of the DM. By deforming the DM, the SH spots due to the DM move laterally, while the spots due to reflections off lens L2 stay the same. By producing a frame, F_d as a difference of the images in the left column in Fig. 2, only useful SH spots are retained. They represent the SH spots for the flat DM and for deformed DM. Then, an additional frame F_Σ is created by adding the frames of the deformed and non-deformed spots. By subtracting F_d from F_Σ another frame Fs is produced. This frame contains the stray reflections only. Then, by subtracting Fs from the deformed and non-deformed original images, SH spots free of stray reflections resulted. A centroiding program was created in Labview. The centroiding was carried out with a basic centroiding technique based on an arbitrary thresholding value. Table 1 shows the variations obtained on the 12 spots.

Table 1. Absolute deviations of SH spots obtained using coherence gating from the SH spots obtained using the conventional SH/WFS, measured in pixels

	TD-LCI		SS-LCI	
SH Spot	Δ X	Δ Y	Δ X	Δ Y
1	0.1	0.1	0.619	0.318
2	0.087	0.221	0.136	1.409
3	0.5	0.214	0.144	0.068
4	0.324	0.051	0.111	0.806
5	0.009	0.102	0.083	0.25
6	0.189	0.161	0.059	0.176
7	0.543	0.214	0.3	0.667
8	1.159	0.25	0.346	0.314
9	0.238	0.143	0.167	0.19
10	0.3	0.433	0	0
11	0.122	0.932	0.044	0.333
12	0.7	0.795	0.205	0.119
Average/column	0.356	0.301	0.185	0.388
Average/method	0.329		0.287	

An average difference of 0.329 is obtained for the TD-LCI method and of 0.287 pixels for the SS-LCI method. The selection of the threshold value affects slightly the centroid position and thus could account for a portion of the difference. The errors are relatively high in both CG versions, ~0.3/8 = 4% from the maximum range, considering that in our case, the maximum range of lateral deviation is plus or minus 8 pixels.

5.3.2. Centroiding errors due to the nonuniform distribution of reference power within the beam section

The accuracy of wavefront sensing is determined by the accuracy of centroiding the spots generated by the SH/WFS on the CCD camera. The distribution of power within the CG-SH spot is skewed by the distribution of reference power over the pixels contributing to that spot. A simple normalization correction consists in dividing the signal strength of each pixel with the square root of the signal obtained with the reference beam on and no object beam.

We performed a simulation considering that the CCD has 256x256 active pixels and there are 16 lenslets covering 16x16 pixels each. Let us consider a Gaussian profile for the reference beam whose intensity distribution is such that the value of the profile at pixels 1 and 255 is either S_{edge} = 0.1 or 0.5 from the value in the middle (at pixel 125).

The maximum error is induced when the SH spots are wide. Let us consider that for an incident plane wavefront, each lenslet projects a Gaussian profile of FWHM = 4 pixels diameter (as an example, commensurate with a base disk of 16 pixels diameter projected within an area of 16x16 pixels allocated to each SH spot). A multiplication of the two Gaussian functions, of the reference beam and of the beam projected by each lens, leads to an asymmetric skewed profile for the most extreme SH spots which differ slightly from a Gaussian. Simulation has shown that for the example considered, the centers of the most

#119017 - $15.00 USD Received 29 Oct 2009; revised 11 Jan 2010; accepted 31 Jan 2010; published 3 Feb 2010

extreme SH spots were shifted 0.013 pixel for $S_{edge} = 0.5$ and by 0.047 pixels for $S_{edge} = 0.5$. Accuracies in the estimation of centroids of 0.007 pixels have been reported [31], therefore the error values obtained in the simulation are significant and normalization is necessary. These shift values are less than an order of magnitude smaller than the average error shift in the centroids of the CG-SH spots in comparison with the positions of the centroids of the conventional SH spots in Table 1. This means that the main source of errors mentioned in paragraph 5.3.1 above is not the non-uniform distribution of reference power.

Normalization of the pixel values with the profile of the reference power ensures that similar spot patterns are obtained by coherence gating to those generated by the conventional method using the same interface optics. However in practice, the power within the reference arm is not perfectly uniform. The beam profile is usually a Gaussian, however, non-uniformities in the beam profile could also be introduced by impurities. This may explain some of the signal variations along the A-scan for the CG-SH/WFS in Fig. 4 and Fig. 5 and the errors reported.

5.4. Choice of parameters for the SS-LCI version

The TD-LCI method provides an *en-face* image of SH spots. The SS-LCI method has the disadvantage that an *en-face* image of SH spots can only be obtained after collecting the whole volume of A-scans. The need for volume acquisition makes the SS method less appealing than the TD method for the specific application discussed here.

However, if the user is not interested in depth resolved aberrations in the sample, but merely in the measurement of aberrations in the system, devoid of any stray reflections, a single *en-face* image of aberrations is sufficient. This limited goal requires less processing time. Further simplification is possible by carefully choosing the OPD value (referred above as δz) where this *en-face* image of aberrations is inferred from. The larger δz, the larger the axial range, ΔZ, required for the SS-LCI method, which needs a proportionally larger number M of frequency steps, with impact on the acquisition time. Therefore, by choosing a small value for δz, faster speed would be achievable. A small δz value is also recommendable due to the decay of sensitivity with OPD in SS-LCI. However, the minimum δz value where the method can reliably be performed depends on several factors.

To illustrate this design issue, let us consider as object the DM and the OPD adjusted to $\delta Z = 55$ microns. DM is here to simulate the top layer of the specimen for instance, to be used as the reflecting layer of choice at OPD = δZ. In Fig. 6, the position of the peak in the A-scan, corresponding to δZ, obtained after FFT is shown for four values of the tuning bandwidth, $\Delta\lambda$. By reducing $\Delta\lambda$ 5 times, from 50 nm to 10 nm, the depth range increases proportionally according to $\Delta Z = 0.25M\lambda^2/\Delta\lambda$. The equivalent coherence length, $l_c = 0.44\ \lambda^2/\Delta\lambda$ characterizes the depth resolution, i.e. the differential distance between adjacent sampling point values on the horizontal axis of the FFT. For $\Delta\lambda = 50$ nm and $\lambda = 0.845$ μm, $l_c \cong 6$ μm. By equivalent coherence length l_c, we mean here the coherence length of an equivalent TD-OCT system excited by an OS with a spectrum width equal to the tuning bandwidth $\Delta\lambda$. The ratio of the axial range ΔZ by the equivalent coherence length, l_c determines the number of sampling points in the FFT, i.e. ≈20 (the same as M/2). This means that the measurement range, ΔZ and l_c vary in the same way with $\Delta\lambda$, therefore the horizontal axis is the same, irrespective of the four experimental values $\Delta\lambda$ in Fig. 6. However, the peak corresponding to δZ, on position $\delta Z/l_c$ on the axis of the graph in Fig. 6 moves from position 11 for $\Delta\lambda = 50$ nm to approx. 2 for $\Delta\lambda = 10$ nm. At such low coordinate value, this peak may not be distinguishable from the very strong peak at OPD = 0 which always exists due to the constant terms before FFT, such as the reference optical power.

#119017 - $15.00 USD Received 29 Oct 2009; revised 11 Jan 2010; accepted 31 Jan 2010; published 3 Feb 2010

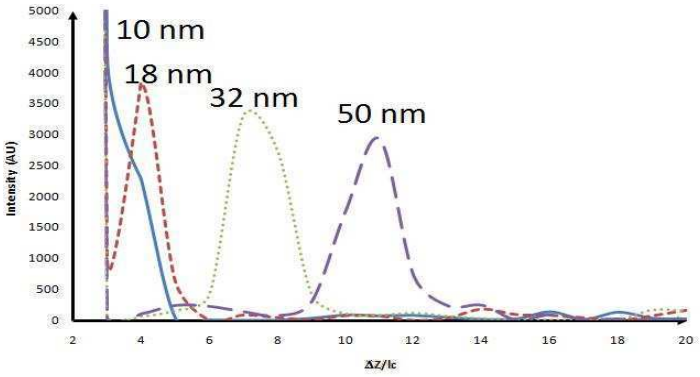

Fig. 6. Graph of the Fourier transformation of the CCD signal for four values of the swept source tuning bandwidth, $\Delta\lambda$, around a central wavelength, λ, of 845 nm and for δZ = 55 μm. The curves are represented starting from $\Delta Z/l_c \approx 3$, due to the large value of peak in zero, whose tail is visible as an almost vertical line.

To make sure that the peak in the A-scan in Fig. 6 is sufficiently distinguishable from the peak at OPD = 0, a safe condition would be that δZ is chosen at least $4l_c$, as shown by the peak for $\Delta\lambda$ = 18 nm. On the other hand, when using small tuning bandwidth, the depth resolution deteriorates. In order to still eliminate the stray reflections, we have to make sure that the depth resolution interval is much smaller than the distance from the working position, δZ, and the axial position of the source of stray reflections. In conclusion, δZ, $\Delta\lambda$, M and the position in depth of the source of stray reflections are inter-related. This connection between such parameters has to be considered when attempting to speed up the process by reducing the number of frames, M. Results have been presented in paragraph 5.1 using M = 40, however, based on the discussion detailed here, higher speed than that reported in paragraph 5.1. can be contemplated by a further decrease of M, giving suitable consideration to the choice of values for δZ and $\Delta\lambda$. A similar reasoning should also be considered when attempting to reduce $\Delta\lambda$, either to allow utilization of a low cost swept source, of reduced tuning bandwidth, or when interested in providing chromatic dependent wavefront measurements, by using subdivisions of the tuning bandwidth of the swept source (as discussed in the paragraph 6.3.2 below).

6. Discussion

This section elaborates further on the design criteria and possible applications of a CG-SH/WFS.

6.1. Acquisition rate

The relatively large time required until data on the wavefront is provided renders the methods presented marginally applicable to moving targets, such as the eye. However, technology is now available at the level where several tracking methods have been reported, which can be used to eliminate the effects of the lateral eye movements [32]. This was proven successfully for both SLO and OCT imaging. Recent reports have also proven the possibility to adjust the OPD in OCT imaging channels [33,34] using a LCI axial tracker. The same principle can obviously be incorporated into the LCI interferometer of any of the two CG implementations here, to reduce the eye axial movement effects. When the CG-SH/WFS is part of an imaging system, the lateral tracker will maintain the beam laterally over the same pixel for both the imaging system and the CG-SH/WFS. However, if the imaging channel is OCT, then the imaging channel and the CG/WFS may need independent axial trackers.

Further improvements in speed may be possible by devising parallel reading arrays using FPGAs [35] and dedicated arrays of photodetectors with parallel reading. A fast full field

#119017 - $15.00 USD Received 29 Oct 2009; revised 11 Jan 2010; accepted 31 Jan 2010; published 3 Feb 2010

OCT system, implementing similar procedures to those used in our TD-LCI version has been applied to the rat eye, using a CMOS camera operating at a frame rate of 250 Hz [30].

The acquisition time of 1 s for the SS-LCI version is similar to the shortest time reported to date on imaging a whole volume of the retina using SS-OCT [36], however the overall time of 3.1 s, with 2.1 s for processing, mentioned in paragraph 5.1.2 render the method unsuitable for measuring moving targets. This duration could be reduced by using a higher performance multiple cores PC or a dedicated DSP board. Recent progress in using graphic processing units performing computation [37] instead of central processing unit may allow for even faster processing speed. The acquisition time, can also be reduced if a similar camera to that in [30], working at 250 Hz is used in the SS-LCI version. This can allow a complete acquisition of the number M = 40 of frames used here at a rate faster than 6 Hz.

As a particular improvement feature, linearization [38] can be avoided if the axial position of operation δZ chosen is shallow, where the nonlinear dependence on the wavenumber can be neglected. From the practice of spectral domain OCT it is known that nonlinear sampling in frequency manifests especially when the OPD is larger than the middle range (peaks loose in amplitude more than expected and shoulders appear). By choosing the OPD value of work at approx. 1/3 of the axial range would be sufficient to ignore the nonlinearity effect. In case the SS-LCI system is used for depth resolved aberrations inside a microscopy sample, then the thickness of the sample determines a minimum number of frames to be acquired. It is known that the sensitivity of the SS-LCI method decreases with OPD. To have sufficient signal at a maximum OPD of 1 mm for instance, the axial range should be at least double, 2 mm. Using again $\Delta Z = 0.25M\lambda^2/(\Delta\lambda)$ for the axial range, this leads to M larger than 600 frames for $\lambda = 0.8$ microns and $\Delta\lambda = 50$ nm. In this case, linearization of data is necessary which increases the time required even more.

6.2. Depth resolution interval

The choice of depth resolution of the LCI method used in the CG-SH/WFS depends on the application. The limits of the depth resolution interval depending on specific application are discussed below.

6.2.1. Superior limit

If the CG-SH/WFS is devised to accomplish the limited goal of stray reflection elimination (and not that of a depth resolved WFS), a low depth resolution capability may be acceptable, consistent with a depth resolution interval of hundreds of microns or even millimeters. Such values could be sufficient to eliminate the effect of stray reflections from lenses in the interface optics of the imaging system. This would allow the use of laser diodes below threshold [39], of much lower cost than superluminescent diodes. Equivalently, the tuning bandwidth of the SS for the SS-LCI version could be smaller, and lower costs tunable sources may be developed in the future.

As little value is envisaged in providing ultra high resolution depth resolved aberration measurements from within a sample, be it retina or a microscopy specimen, a much larger coherence length of the source can be tolerated in CG-SH/WFS than in OCT imaging. Therefore, low cost laser diodes below threshold may be again used in the TD implementation or smaller tuning bandwidth sources in the SS implementation. For instance, if a priori information exists about the sample, which has two major layers at different depths in terms of reflectivity value or birefringence values, it may be sufficient to provide aberration information from depth intervals separated by no more than the depth interval between such layers.

However, more research is required to establish the influence of speckle when the source presents narrow linewidth. A possible solution for reducing the speckle effects is increasing the number of phase steps in the TD method and the number of frequency steps in the SS

#119017 - $15.00 USD Received 29 Oct 2009; revised 11 Jan 2010; accepted 31 Jan 2010; published 3 Feb 2010

method used and therefore a trade-off should be evaluated between the advantage of lower cost and increased collection and processing time.

6.2.2. Lower limit

There is also a limit in terms of the smallest achievable resolution interval. This is determined by the curvature of the coherence gate at the back of the lenslet array.

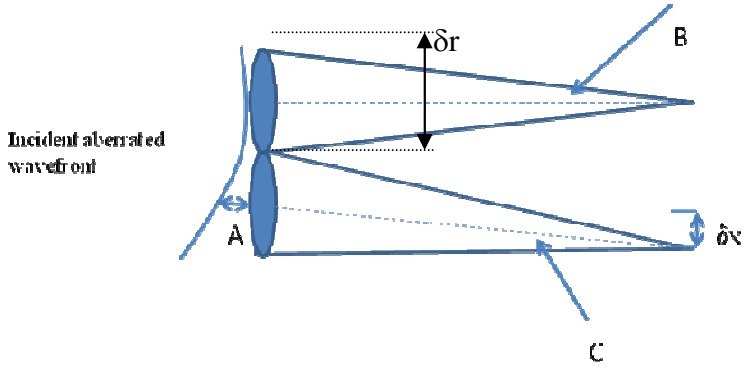

Fig. 7. Components of the optical paths in the object arm. B: optical path length for the SH spot corresponding to a non-aberrated part of the wavefront; C: optical path length for the SH spot corresponding to an aberrated part of the wavefront; δx represents the lateral deviation of the SH spot from the reference grid node.

In Fig. 7, A is the deviation of the wavefront due to its tilt from the ideal plane. Due to this, the SH focus of the beamlet is deviated to a distance δx from the non-aberrated position measured in the CCD plane, and the beamlet traverses distance C from the lenslet. As seen in Fig. 7, the difference in length between the aberrated and non-aberrated case can lead to an optical path difference:

$$D = (C - B) + A \tag{6}$$

where C is:

$$C = \sqrt{\delta x^2 + B^2} \tag{7}$$

The maximum deviation δx can be r, the radius of the lenslet. If D exceeds half of the coherence length, the SH spot can be out of coherence and thus eliminated by the coherence gate in TD-LCI and out of the inferred *en-face* frame in the SS-LCI case. This shows that the coherence length and the focal length of the lenslets need to be selected carefully. For a lenslet array with a focal length of 7.5 mm and a pitch of 200 μm, the maximum distance for C is around 7.5007 mm so the difference between C and B is 0.7 μm. In a SH/WFS, the slope of the wavefront is equal to:

$$m = \frac{\delta x}{f} \tag{8}$$

For the example above, this gives a value for the slope of 0.0133. However, the slope of the wavefront can also be inferred as:

$$m = \frac{A}{2r} \tag{9}$$

From (8) and (9),

#119017 - $15.00 USD Received 29 Oct 2009; revised 11 Jan 2010; accepted 31 Jan 2010; published 3 Feb 2010

$$A_{\max} = \frac{2r^2}{f} \tag{10}$$

which gives:

$$D_{\max} = \sqrt{r^2 + f^2} - f + \frac{2r^2}{f} = 4.4\ microns \tag{11}$$

This distance is smaller than the coherence length of the SLD, 17 μm used in the TD case and the equivalent coherence length of 6 μm for 50 nm tuning bandwidth and 30 μm for 10 nm tuning bandwidth used in Fig. 6. This example shows that care has to be taken when extending technology of high depth resolution LCI [40] to the coherence gating principle applied to a SH/WFS.

The calculation above refers to the OPD variation across a lenslet pair. Over the entire wavefront, a Peak to Valley difference of several microns is not unusual. Including tilt, the peak to valley of a wavefront could be even larger. This would result in some of the SH spots in the system being outside the coherence gate.

6.3. Spectral variation of aberrations

Chromatic aberrations [14] are often ignored in the practice of wavefront sensing. In previous WFS studies, a series of filters to select the measurement wavelength have been used one after another, as described in [41]. Defocus can change by up to 0.4 diopters in the human eye when the wavelength is varied within a 200 nm range in the IR range centered at 800 nm [42]. The evaluation of chromatic aberration is therefore essential for achieving good performance in high resolution imaging of the retina. The SS-LCI version of the CG-SH/WFS presented may find applications in two possible directions, as outlined below.

6.3.1. Synchronous chromatic compensation with SS tuning of the CG-SHS

When tuning the SS, correction for the chromatic aberration in the interface optics or in the sample can be implemented in synchronism. In the simplest case, the aberration refers to the focus change with wavelength. It may be possible using a sufficiently fast electrically controlled lens to adjust the chromatic focus variation while sweeping the wavelength in the SS-CG/WFS. However, more research is required to establish the values of such a method in comparison with the use of an achromatiser [40].

6.3.2. Spectroscopic characterization

An alternative use of the SS-LCI principle is where the tuning bandwidth employed in constructing the A-scans is adjusted to a value smaller than the achievable tuning bandwidth of the SS used. The main band of the SS is divided, let us say into N subintervals, for instance 100 nm can be divided into N = 5 subintervals, 20 nm each. The SS-LCI based CG-SH/WFS operates within a bandwidth of 20 nm with wavelength centered on either of the 5 such subintervals. Spectroscopic information on aberrations is achieved in this way at 5 different wavelengths by inferring an *en-face* image of aberrations at the chosen OPD according to paragraph 5.4 for each of the 5 subintervals. Opportunity in using again a controllable lens or an achromatizer, as discussed above remains to be researched.

7. Conclusions

In this paper we demonstrated that interference between the focused beams resulting from lenslet arrays used in a SH/WFSs and a collimated beam can be successfully handled to provide depth resolved spots. Two methods of coherence gating have been presented for providing depth resolved spots. A TD-LCI method leads to an *en-face* image of spots using phase shifting interferometry. A SS-LCI method provides A–scans for each pixel in the 2D

#119017 - $15.00 USD Received 29 Oct 2009; revised 11 Jan 2010; accepted 31 Jan 2010; published 3 Feb 2010

photodetector array and an *en-face* image of SH spots is obtained after post-processing of the volume of A-scans.

Both methods have been used to demonstrate the operation of a CG-SH/WFS which can work under large stray reflections in the interface optics and therefore could lead to wavefront sensing assisted AO microscopy, reduction of the layout size of AO assisted imaging instruments and to an improvement in performance. The two proof of concept configurations demonstrated real time operation, which make them superior to the method using a virtual lenslet array [21] or iterative algorithms [43]. The need to collect several images for both versions of CG-SH/WFSs presented, slows down the data rate and therefore the time reported is marginally sufficient for imaging the eye, faced with micro-saccades and head movements (10 Hz for the TD version and 1 Hz for the SS version). Future work is required to make such principles working faster to be able to cope with the involuntary eye movements.

Centroiding was applied to perform a comparison of SH spots obtained with the conventional SH/WFS and with the two principles of CG-LCI. This has shown that the SH spot patterns obtained were similar up to an average error of ~0.3 pixels which determines more than 4% error. These results however were obtained using a minimum number of frames required for the two methods to work. The TD version employs phase shifting interferometry, where the minimum number of steps is 3 and we used 4. In the SS version, smaller number of frames than 40 would have reduced the amplitude of the peak in the A-scan (due to the decay with depth of sensitivity specific for spectral domain LCI). Larger number of frames in both methods may lead to improvement in the accuracy determination of the wavefront. It may be possible that some of the errors in the lateral shifts of CG SH spots from the conventional SH spots be generated by speckle. Therefore, more research is required to evaluate the trade off between speckle average and speed, when choosing the number of frames.

No processing was performed in this paper to infer the aberrations. The next step is to incorporate such a CG-SH/WFS into an imaging system, collect the spot pattern from a scattering sample and correct for the aberrations using a corrector under a closed AO loop. A unique direction opened by the methods presented is that of assembling AO configurations using lenses in the interface optics, compatible with double path correction. As demonstrated here, elimination of large stray reflections will allow a CG-SH/WFS to operate under reflections from microscope objectives and microscope slides. If such a configuration is made operational, it will be possible to evaluate how aberrations vary with depth in thick microscopy samples.

Acknowledgement

Support from Superlum is acknowledged which lent us the Sweeper to demonstrate the CG-SH/WFS based on SS-LCI. ST acknowledges the Marie Curie training site, MEST-CT-2005-020353.

#119017 - $15.00 USD Received 29 Oct 2009; revised 11 Jan 2010; accepted 31 Jan 2010; published 3 Feb 2010